Non-monotonic effect of growth temperature on carrier collection in SnS solar cells

Non-monotonic effect of growth temperature on carrier collection in SnS solar cells

R. Chakraborty,[1] V. Steinmann, [1] N. M. Mangan, [1] R. E. Brandt, [1] J. R. Poindexter, [1] R. Jaramillo, [1] J. P. Mailoa, [1] K. Hartman, [1] A. Polizzotti, [1] C. Yang, [2] R. G. Gordon, [2] T. Buonassisi,[1]

[1]*Massachusetts Institute of Technology, Cambridge, MA, 02139, USA*

[2]*Harvard University, Cambridge, MA, 02138, USA*

We quantify the effects of growth temperature on material and device properties of thermally evaporated SnS thin-films and test structures. Grain size, Hall mobility, and majority-carrier concentration monotonically increase with growth temperature. However, the charge collection as measured by the long-wavelength contribution to short-circuit current exhibits a non-monotonic behavior: the collection decreases with increased growth temperature from 150°C to 240°C and then recovers at 285°C. Fits to the experimental internal quantum efficiency using an opto-electronic model indicate that the non-monotonic behavior of charge-carrier collection can be explained by a transition from drift- to diffusion-assisted components of carrier collection. The results show a promising increase in the extracted minority-carrier diffusion length at the highest growth temperature of 285°C. These findings illustrate how coupled mechanisms can affect early-stage device development, highlighting the critical role of direct materials property measurements and simulation.

Tin (II) sulfide (SnS) is a promising Earth-abundant thin-film solar absorber material because of its high absorption coefficient in the visible wavelengths,[1–5] tunable hole carrier density in the range 10^{15} to 10^{18} cm^{-3},[1,6] and potential for high-throughput manufacturing.[5] In recent years, the conversion efficiency of SnS-based solar cells has considerably improved from 1.3% to 4.36%.[1,7–11] However, the record efficiency still pales in comparison to the theoretical maximum efficiency[a] of SnS, 32%.[12] As a step towards understanding the loss mechanisms at play, the present work focuses on the measurement and modeling of carrier collection and photocurrent in SnS devices. The methodology used here to connect material properties to device performance generalizes to other thin-film absorber materials in early-stage device development.

We recently reported on thermally evaporated SnS-based solar cells with a short-circuit current (J_{SC}) of 20.6 mA/cm^2.[5] This is among the highest J_{SC} in the literature for SnS-based solar cells,[10,11] yet is still less than half of the theoretical maximum of 43.3 mA/cm^2.[5] An analysis of the external quantum efficiency revealed the leading loss mechanism: 19% of all incident photons are lost to recombination, mostly at long wavelengths (>700 nm).[5] Improving charge-carrier collection in the SnS layer is a critical step toward improving the short-circuit current to levels that justify industrial scale-up.

For other thermally evaporated thin-film solar cell materials such as cadmium telluride and copper (indium, gallium) (diselenide, disulfide), the growth temperature T_g is a critical process parameter affecting charge-carrier collection in devices.[13,14] Although the effect of T_g on crystalline texture, grain size, electrical transport properties, and optical properties of SnS thin films has been studied extensively,[15–19] its effect on charge-carrier collection has not yet been directly measured through a working SnS photovoltaic device.

[a] Assumes a bandgap of 1.1 eV.

In this work, we determine the effect of growth temperature T_g on the structural and electrical properties of thermally evaporated SnS films. We then measure the internal quantum efficiency (IQE) of devices using a previously developed device stack.[5] IQE probes the collection efficiency due to drift and diffusion, allowing us to analyze the transport properties of SnS under different processing conditions. By increasing the SnS growth temperature from 150 to 285°C, we traverse through a local minimum in long-wavelength carrier collection, a behavior we attribute to the combined effects of a varying SnS majority-carrier concentration and minority-carrier diffusion length. A monotonic increase in carrier concentration with increasing growth temperature leads to decreasing drift-assisted carrier collection. This causes a decrease in total collection up to the highest growth temperature of 285°C. Despite the decrease in drift-assisted collection at 285°C, we see a recovery in total long-wavelength carrier collection due to an improvement in minority-carrier diffusion length. This suggests that the films grown at the highest temperature have a lower density of lifetime-limiting bulk defects.

The SnS thin films are grown via thermal evaporation on $Si/SiO_2/Mo$ substrates at four substrate temperatures: 150, 200, 240, and 285°C. The deposition rate is held at 1–2 Å/s. Substrate temperatures higher than 285°C result in re-evaporation of SnS from the substrate due to the low deposition rate and large source-to-substrate distance (10 cm) in our thermal evaporation system. All films are subsequently annealed at 400°C in 4% H_2S atmosphere (N_2 balance) at 28 Torr for 60 minutes to promote grain growth. Re-evaporation is strongly suppressed during annealing,[20] presumably because the high total pressure limits re-evaporation. The post-annealed film thicknesses range from 886-1204 nm due to differences in surface topology and error in deposition rate measurement. Devices are fabricated with each annealed film using a previously reported procedure.[21] The device stack includes a thin SnO_2 layer on the SnS surface and a Zn(O,S):N *n*-type buffer layer. Each sample contains 11 devices defined by a shadow-masked ITO pattern. Further details on the preparation of SnS powder, preparation of

Si/SiO_2/Mo substrates, thermal evaporation and annealing parameters, and device fabrication steps are described in prior work.[21]

We first study the impact of T_g on the structural and electronic properties of SnS thin-films, summarized in Figure 1. The morphology of the SnS films are characterized by field-emission scanning electron microscopy (Zeiss, Ultra-55), and grain areas are extracted by analyzing manual traces[20] using the image processing software ImageJ.[22] The micrographs (Figure 1a) indicate a variation in packing density of grains. As T_g increases, intergranular voids decrease in size and frequency. Figure 1b shows a box plot representing the distribution of in-plane grain diameters (assuming circular grains) for each growth temperature. The median grain diameter increases monotonically with T_g, ranging from 191 nm at $T_g = 150°C$ to 383 nm at $T_g = 285°C$. The grain diameter distribution profile also changes as a function of T_g. As T_g increases, the midspread of grain diameters increases, accompanied by an increasingly positive skew in the distribution. For example, the upper quartile grain size for $T_g = 150°C$ is 269 nm, as compared to 616 nm for $T_g = 285°C$. All of these morphological trends are observed despite an identical 1-hr post-deposition anneal at 400°C for all samples. This suggests that the as-grown film morphology may kinetically limit the grain-growth during the subsequent anneal step.

Figure 1c and 1d show the results of Hall effect measurements carried out on SnS sister samples grown on Si/SiO_2 wafers. All films were *p*-type, and the hole concentration increased monotonically with T_g from 6.3×10^{15} to 3.1×10^{16} cm^{-3}. The hole concentration is likely controlled by the concentration of doubly-ionized Sn vacancies, which are predicted to be shallow acceptors.[23] The film resistivity decreased from 49 to 6.3 Ω-cm. Hole mobility tended to increase with T_g, ranging from 20.1 to 31.6 $cm^2/V \cdot s$. The upward trend in grain size and mobility with T_g is consistent with decreasing grain boundary scattering,[24] but other intragranular scattering processes may also limit mobility. Notably, the dependence of electrical properties on T_g persist despite a post-deposition anneal at 400°C.

External quantum efficiency measurements are performed (PV Measurements Model QEX7) at room temperature without light or voltage bias. Internal quantum efficiency is calculated by $\mathrm{IQE} = \frac{\mathrm{EQE}}{1-R}$, where R is the reflectivity of the device stack as measured by a spectrophotometer (Perkins Elmer Lambda 950). Figure 2 shows the average IQE from all rectifying devices on each substrate. Below 450 nm, the IQE drops sharply due to optical absorption in the Zn(O,S):N and ITO layers.[5] In the wavelength range 450-700 nm, the IQE varies across growth temperatures. Although this short-wavelength region is sensitive to carrier collection within 100 nm from the SnS/Zn(O,S):N interface (as $\alpha > 10^5$ cm^{-1} for these wavelengths), this region is also particularly sensitive to errors in the reflectivity measurement due to pronounced optical interference in the ITO and Zn(O,S):N layers. In contrast, the long-wavelength region 700-950 nm is more sensitive to changes in carrier collection throughout the bulk, because for these wavelengths the absorption coefficient α is as low as 10^4 cm^{-1} and film thicknesses are $\sim 10^{-4}$ cm. Moreover, interference fringes in the reflectivity spectrum due to the ITO and Zn(O,S):N layers are less pronounced for wavelengths beyond 700 nm. Thus, we restrict our analysis of carrier collection to the long-wavelength region 700-950 nm. In this region, we observe an unexpected trend: the magnitude of IQE varies non-monotonically with T_g. Figure 3a shows the integrated IQE in the long-wavelength range in terms of the current density

$$J_{\mathrm{IQE,lw}} = \int_{700\ \mathrm{nm}}^{950\ \mathrm{nm}} \mathrm{IQE}(\lambda)\ \phi_{AM1.5}(\lambda)\ \frac{\lambda}{hc}\ d\lambda \qquad (1)$$

where $\phi_{AM1.5}(\lambda)$ is the AM1.5 spectral irradiance. As growth temperature increases, $J_{\mathrm{IQE,lw}}$ decreases from 8.4 mA/cm^2 at $T_\mathrm{g} = 150$°C, to 6.3 mA/cm^2 at $T_\mathrm{g} = 240$°C, and then increases back to 8.4 mA/cm^2 at the highest growth temperature of 285°C (Figure 3a).

We hypothesize that this non-monotonic behavior in long-wavelength IQE with temperature is due to the combined effects of a varying majority-carrier (hole) concentration p and minority-carrier diffusion length L_diff. The depletion width decreases with increasing p, reducing the distance over which the

internal electric field assists collection of minority electrons from the SnS bulk. That is, a lower hole concentration should result in a larger photo-generated carrier collection because there is a higher minority-carrier drift current. Figure 3b shows the depletion widths computed using measured hole carrier concentrations and an analytic expression for heterojunctions.[20,25] The SnS film grown at the lowest temperature of 150°C has the lowest p (Figure 1d), the largest depletion width, and thus the most drift-assisted collection. As carrier concentration increases with T_{g}, we expect a decrease in drift-assisted collection due to a shrinking depletion width. This trend in expected drift-assisted collection is consistent with the trend in $J_{\mathrm{IQE,lw}}$ for $T_g \leq 240$°C. However, for the highest growth temperature of 285°C, we observe a recovery of $J_{\mathrm{IQE,lw}}$ despite the relatively small depletion width. One possible mechanism for the relatively high $J_{\mathrm{IQE,lw}}$ at 285°C is by an enhancement of L_{diff}.

We verify this hypothesis by implementing a one-dimensional opto-electronic model in SCAPS-1D[26] and fitting to the experimental long-wavelength IQE.[20] With the model, we demonstrate that the decreasing trend in $J_{\mathrm{IQE,lw}}$ for growth temperatures up to 240°C is caused by an increasing hole concentration, while the resurgence in $J_{\mathrm{IQE,lw}}$ at 285°C is driven by an increase in L_{diff}. As inputs to the simulation, we use material parameters extracted from experimental data on the here-studied samples in conjunction with literature values.[20] Within the defined parameter space, the minority-carrier mobility μ_e and minority-carrier lifetime τ_n affect $J_{\mathrm{IQE,lw}}$ equivalently. We aim to fit the simulated long-wavelength (700–950 nm) IQE to experimental data by using the $\mu_e\tau_n$ product as the effective fitting parameter, and then extract the fitted diffusion length $L_{\mathrm{diff}} = \sqrt{\frac{kT}{q}\mu_e\tau_n}$.[20]

The fitted diffusion lengths are shown by the filled squares in Figure 3c. The error bars in Figure 3c take into account both uncertainty in material parameters from the literature, as well as the effect of varying T_{g}-dependent parameters other than hole concentration.[20] For the lowest growth temperature of 150°C, the fitted diffusion length ranges from 88–135 nm. Remarkably, the L_{diff} ranges for $T_{\mathrm{g}} = 200$°C and

240°C statistically overlap with the range for $T_g = 150$℃, implying that the change in hole concentration alone is sufficient to explain the change in $J_{IQE,lw}$ for growth temperatures up to 240°C. However, the fitted diffusion lengths for T_g =285°C range from 172–228 nm, well above the ranges for lower growth temperatures. Thus, even accounting for variation of other parameters, the recovery in $J_{IQE,lw}$ at $T_g = 285$°C cannot be explained without an increase in L_{diff} of the films deposited at this temperature. We note that the hole concentration measurements are performed on different substrates from those used for device measurements. Although this could result in quantitative differences in p and the fitted L_{diff}, the trends in p and L_{diff} as a function of T_g are likely unaffected.[20] As a check, we also consider the effects of a varying surface roughness and absorption coefficient on $J_{IQE,lw}$, and find that they are insufficient to account for the variation in measured $J_{IQE,lw}$.[20]

Because the Hall mobility increases by only 2.9% from $T_g = 240$°C to 285°C, the rise in L_{diff} at 285°C is likely driven by an enhancement of effective minority-carrier lifetime. Recalling that the grain size is highest for $T_g = 285$°C, a reduction in grain boundary recombination may contribute to the increase in L_{diff}.[27] However, grain size tends to increase monotonically with temperature, whereas the fitted L_{diff} stays nearly constant for $T_g < 285$℃. Thus, grain boundary recombination alone does not explain the trend in fitted L_{diff} . Instead, we suspect that a reduction of intragranular defect density is responsible for the enhancement of minority-carrier lifetime at $T_g = 285$℃.

In optimizing SnS bulk properties for maximum carrier collection, we would ideally benefit from both drift and diffusion. Figure 4 is a contour plot of simulated $J_{IQE,lw}$ for a range of SnS hole concentrations and diffusion lengths, with the results of the present study appropriately overlayed in the parameter space.[20] Here it is more easily seen how as T_g increases, we traverse through the parameter space in a way that produces lower $J_{IQE,lw}$ at the intermediate temperatures. Additionally, we should aim for both lower carrier concentrations (towards 10^{15} cm^{-3}) and higher diffusion lengths to achieve long-

wavelength current densities approaching the theoretical maximum of $J_{\mathrm{IQE,lw}} = 15.0$ mA/cm^2. It is also important to note a qualitative difference in the effect of hole concentration versus that of diffusion length on $J_{\mathrm{IQE,lw}}$. Increasing L_{diff} increases both diffusive and drift collection and is especially effective at improving carrier collection. In contrast, decreasing p can only increase collection by enlarging the depletion region and has a more limited improvement capacity. As the carrier concentration is decreased, the loss in current due to the series resistance of SnS counteracts the benefit of drift-assisted collection. Consequently, for a given diffusion length, the net benefit of decreasing p diminishes as p is lowered. We note that while the IQE measurements focus exclusively on the short-circuit point, the SnS hole concentration also affects the open-circuit voltage and fill factor. The SnS hole concentration should thus be optimized not only for short-circuit carrier collection, but for overall device efficiency. Work is ongoing in co-optimizing growth and annealing conditions to allow tunable carrier concentration while maximizing diffusion lengths.

In summary, we have shown that by increasing growth temperature from 150 to 285°C, we traverse through a local minimum in current density at long wavelengths due to the combined effects of a varying carrier concentration and diffusion length. The hole concentration monotonically increases with increasing growth temperature, which leads to decreasing drift-assisted carrier collection. At the highest growth temperature, we observe a recovery of the carrier collection due to an increase in diffusive minority-carrier transport. Higher carrier collection may be achievable by simultaneously decreasing carrier concentration and increasing diffusion length. The fact that the trends in grain morphology, carrier concentration, and extracted diffusion length are observed after a post-growth annealing step of 400°C in H_2S ambient highlights the importance of defect engineering during thin-film growth to achieve optimum bulk material properties. The increase in diffusive carrier transport at 285°C is promising, as it suggests we may achieve even higher diffusion lengths and enhanced device performance with growth temperatures beyond 285°C. Higher substrate temperatures can be attained by

increasing the source temperature and decreasing the source-substrate distance to increase the SnS adatom flux. Ideally, a close-space sublimation geometry would be employed, allowing far higher growth temperatures. These steps to increase growth temperature may be critical to achieve high-quality SnS thin films which ultimately improve the efficiency of SnS-based photovoltaic devices.

Acknowledgements

The authors are thankful to Mariela Lizet Castillo for helping with substrate preparation. The authors also thank Luisa Barrera and Kelsey Doolittle for helping with the grain size analysis and anisotropic calculations, respectively. This work is supported by the U.S. Department of Energy through the SunShot Initiative under contract DE-EE0005329, and by Robert Bosch LLC through the Bosch Energy Research Network under grant 02.20.MC11. V. Steinmann, R. Jaramillo, K. Hartman, and R.E. Brandt acknowledge the support of the Alexander von Humboldt foundation, a DOE EERE Postdoctoral Research Award, an Intel PhD Fellowship, and an NSF GRFP Fellowship respectively. This work made use of the MRSEC Shared Experimental Facilities at MIT that is supported by the National Science Foundation (NSF) under award DMR-08-19762, and the Center for Nanoscale Systems that is supported by the NSF under award ECS-0335765.

RC led the experimental planning, film characterization, and data analysis. VS aided in experimental planning, sample fabrication, and device characterization. RC, VS, NMM, and REB wrote the paper. JRP took the IQE data and helped with initial IQE analysis which led to the full device simulations. NMM and REB assisted with the device simulations and interpretation of the simulation results. RJ carried out the AFM measurements, helped interpret the 2D optical simulation results, and contributed to device fabrication. JPM carried out the 2D optical simulations. KH, AP, and CY were involved with sample fabrication. RGG and TB led the overall project as the PIs of the collaborating labs at Harvard and MIT, including assisting the team with data interpretation, structuring, and presentation.

Figures

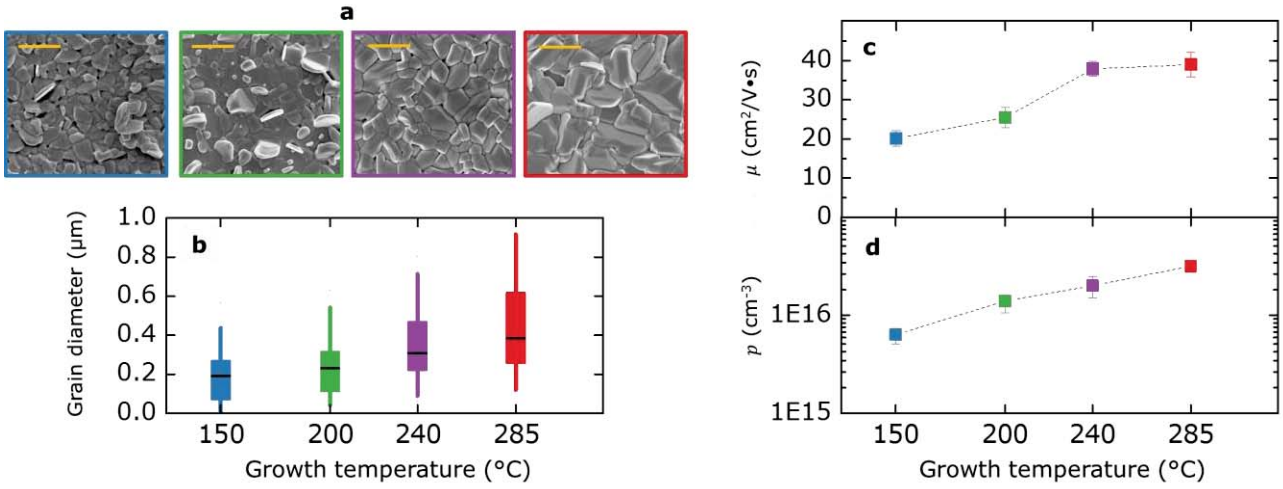

Figure 1. Experimental data on structural and electrical properties. (a) Plan-view SEM, showing increasing grain size with growth temperature (increasing temperature left to right: 150°C in blue, 200°C in green, 240°C in purple, 285°C in red). Scale bar indicates 1 μm. (b) Distribution of post-annealed grain diameters tending towards larger grains with increasing growth temperature. Black horizontal line indicates median; edges of box indicate 25th and 75th percentiles; whiskers indicate 5th and 95th percentiles. (c),(d) Hall mobility and carrier concentration, respectively, both increasing with growth temperature. Error bars indicate propagation of experimental uncertainty in thickness measurement by SEM and contact placement.

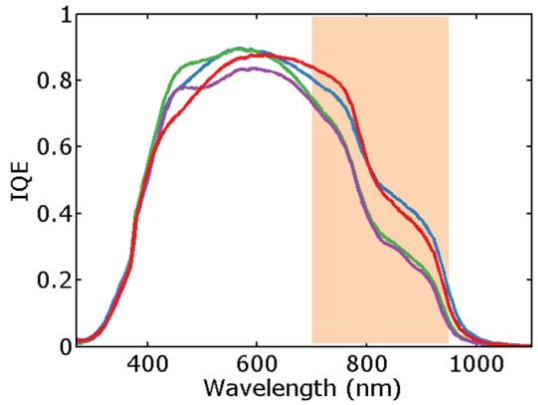

Figure 2. Measured internal quantum efficiency of SnS thin-film devices for the four growth temperatures (150°C in blue, 200°C in green, 240°C in purple, 285°C in red). The highlighted region indicates the wavelength range (700–950 nm) which was fitted using a one-dimensional opto-electronic model in SCAPS-1D.

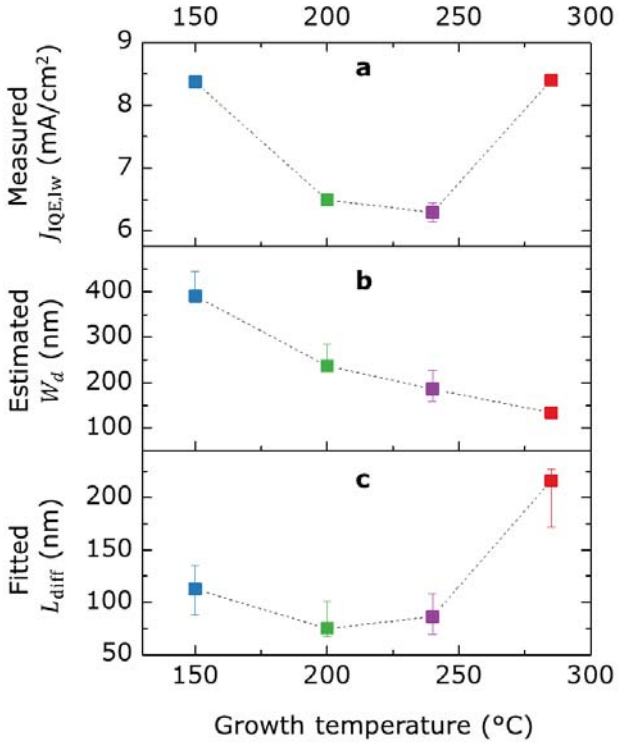

Figure 3. SnS thin-film device parameters as a function of growth temperature (150°C in blue, 200°C in green, 240°C in purple, 285°C in red). (a) Current density $J_{\mathrm{IQE,lw}}$ extracted from experimental IQE by integrating over the long-wavelength regime (700–950 nm). (b) Estimated depletion width W_d based on the measured hole concentration. Error bars represent uncertainty in material parameter values. (c) Fitted diffusion length L_{diff} based on a one-dimensional opto-electronic model in SCAPS-1D. Error bars take into account both uncertainty in material parameters from the literature, as well as the effect of varying T_{g}-dependent parameters other than hole concentration.

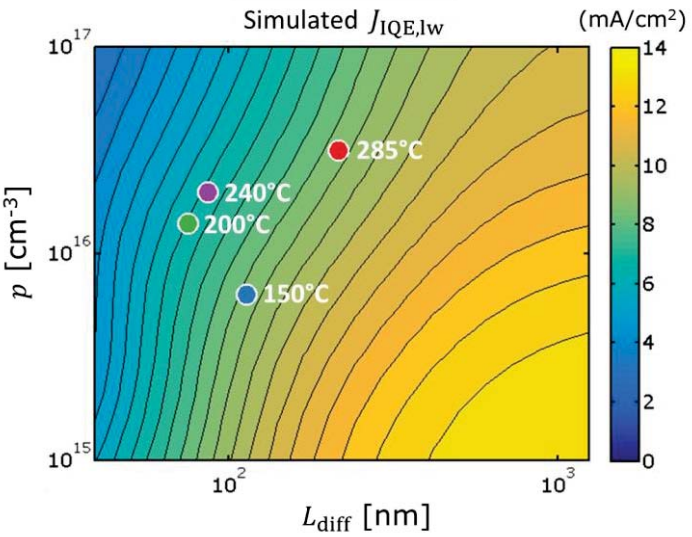

Figure 4. Contour plot of the current density $J_{\mathrm{IQE,lw}}$ as a function of diffusion length L_{diff} (abscissa) and hole concentration p (ordinate). The experimental data points representing each growth temperature are positioned based on measured carrier concentration and fitted diffusion length. Within the parameter space plotted, lower p and higher L_{diff} tend to increase $J_{\mathrm{IQE,lw}}$.

References

[1] K. Ramakrishna Reddy, N. Koteswara Reddy, and R. Miles, Sol. Energy Mater. Sol. Cells **90**, 3041 (2006).

[2] P. Sinsermsuksakul, J. Heo, W. Noh, A.S. Hock, and R.G. Gordon, Adv. Energy Mater. **1**, 1116 (2011).

[3] A. Tanusevski and D. Poelman, Sol. Energy Mater. Sol. Cells **80**, 297 (2003).

[4] K. Hartman, J.L. Johnson, M.I. Bertoni, D. Recht, M.J. Aziz, M. a. Scarpulla, and T. Buonassisi, Thin Solid Films **519**, 7421 (2011).

[5] V. Steinmann, R. Jaramillo, K. Hartman, R. Chakraborty, R.E. Brandt, J.R. Poindexter, Y.S. Lee, L. Sun, A. Polizzotti, H.H. Park, R.G. Gordon, and T. Buonassisi, Adv. Mater. **26**, 7488 (2014).

[6] H. Noguchi, A. Setiyadi, H. Tanamura, T. Nagatomo, and O. Omoto, Sol. Energy Mater. Sol. Cells **35**, 325 (1994).

[7] A. Schneikart, H.-J. Schimper, A. Klein, and W. Jaegermann, J. Phys. D. Appl. Phys. **46**, 305109 (2013).

[8] T. Ikuno, R. Suzuki, K. Kitazumi, N. Takahashi, N. Kato, and K. Higuchi, Appl. Phys. Lett. **102**, 193901 (2013).

[9] P. Sinsermsuksakul, K. Hartman, S. Bok Kim, J. Heo, L. Sun, H. Hejin Park, R. Chakraborty, T. Buonassisi, and R.G. Gordon, Appl. Phys. Lett. **102**, 053901 (2013).

[10] H.H. Park, R. Heasley, L. Sun, V. Steinmann, R. Jaramillo, K. Hartman, R. Chakraborty, P. Sinsermsuksakul, D. Chua, T. Buonassisi, and R.G. Gordon, Prog. Photovoltaics Res. Appl. **20**, (2014).

[11] P. Sinsermsuksakul, L. Sun, S.W. Lee, H.H. Park, S.B. Kim, C. Yang, and R.G. Gordon, Adv. Energy Mater. **4**, (2014).

[12] S. Siebentritt, Sol. Energy Mater. Sol. Cells **95**, 1471 (2011).

[13] C.. Ferekides, D. Marinskiy, V. Viswanathan, B. Tetali, V. Palekis, P. Selvaraj, and D.. Morel, Thin Solid Films **361-362**, 520 (2000).

[14] W.N. Shafarman and J. Zhu, Thin Solid Films **361**, 473 (2000).

[15] M. Devika, N. Koteeswara Reddy, D. Sreekantha Reddy, Q. Ahsanulhaq, K. Ramesh, E.S.R. Gopal, K.R. Gunasekhar, and Y.B. Hahn, J. Electrochem. Soc. **155**, H130 (2008).

[16] M. Devika, K.T. Ramakrishna Reddy, N. Koteeswara Reddy, K. Ramesh, R. Ganesan, E.S.R. Gopal, and K.R. Gunasekhar, J. Appl. Phys. **100**, 023518 (2006).

[17] Y. Guo, W. Shi, Y. Zhang, L. Wang, and G. Wei, Proc. SPIE **6984**, 69841P (2008).

[18] R.W. Miles, O.E. Ogah, G. Zoppi, and I. Forbes, Thin Solid Films **517**, 4702 (2009).

[19] P. a. Nwofe, K.T.R. Reddy, G. Sreedevi, J.K. Tan, I. Forbes, and R.W. Miles, Energy Procedia **15**, 354 (2012).

[20]*See Supplementary Material at [doi] for Justification of 1-D Model and Details on Material Parameter Values.* (n.d.).

[21] R. Jaramillo, V. Steinmann, C. Yang, K. Hartman, R. Chakraborty, J.R. Poindexter, M.L. Castillo, R. Gordon, and T. Buonassisi, J. Vis. Exp. (2015).

[22] M.D. Abràmoff, P.J. Magalhães, and S.J. Ram, Biophotonics Int. **11**, 36 (2004).

[23] J. Vidal, S. Lany, M. d'Avezac, A. Zunger, A. Zakutayev, J. Francis, and J. Tate, Appl. Phys. Lett. **100**, 032104 (2012).

[24] J.W. Orton and M.J. Powell, Reports Prog. Phys. **43**, 1263 (1980).

[25] R. Scheer and H.-W. Schock, *Chalcogenide Photovoltaics: Physics, Technologies, and Thin Film Devices* (Wiley-VCH, 2011).

[26] M. Burgelman, P. Nollet, and S. Degrave, Thin Solid Films **361**, 527 (2000).

[27] H.C. Card and E.S. Yang, IEEE Trans. Electron Devices **24**, 397 (1977).